AGU PUBLICATIONS

Geophysical Research Letters

RESEARCH LETTER
10.1002/2013GL059130

Key Points:
- The dynamo current forms in a torus shape due to the $\vec{E} \times \vec{B}$ drift of electrons
- Asymmetries in the electric field are due to the collision-driven ion dynamics
- Magnetized region can alter charge carrier motion from lower to upper atmosphere

Supporting Information:
- Readme
- Figure S1
- Figure S2
- Text S1

Correspondence to:
J. A. Riousset,
riousset@gatech.edu

Citation:
Riousset, J. A., C. S. Paty, R. J. Lillis, M. O. Fillingim, S. L. England, P. G. Withers, and J. P. M. Hale (2014), Electrodynamics of the Martian dynamo region near magnetic cusps and loops, *Geophys. Res. Lett.*, *41*, 1119–1125, doi:10.1002/2013GL059130.

Received 22 DEC 2013
Accepted 25 JAN 2014
Accepted article online 29 JAN 2014
Published online 22 FEB 2014

Electrodynamics of the Martian dynamo region near magnetic cusps and loops

Jeremy A. Riousset[1], Carol S. Paty[1], Robert J. Lillis[2], Matthew O. Fillingim[2], Scott L. England[2], Paul G. Withers[3], and John P. M. Hale[1]

[1]School of Earth and Atmospheric Sciences, Georgia Institute of Technology, Atlanta, Georgia, USA, [2]Space Sciences Laboratory, University of California, Berkeley, California, USA, [3]Astronomy Department, Boston University, Boston, Massachusetts, USA

Abstract Strong and inhomogeneous remanent magnetization on Mars results in a complex pattern of crustal magnetic fields. The geometry and topology of these fields lead to atmospheric electrodynamic structures that are unique among the bodies of the solar system. In the atmospheric dynamo region (~100–250 km altitude), ions depart from the gyropath due to collisions with neutral particles, while electron motion remains governed by electromagnetic drift. This differential motion of the charge carriers generates electric currents, which induce a perturbation field. The electromagnetic changes ultimately alter the behavior of the local ionosphere beyond the dynamo region. Here we use multifluid modeling to investigate the dynamics around an isolated magnetic cusp and around magnetic loops or arcades representative of the magnetic topology near, for example, Terra Sirenum. Our results show consistent, circular patterns in the electric current around regions with high local field strength, with possible consequences on atmospheric escape of charged particles.

1. Introduction

The Mars Global Surveyor (MGS) mission revealed the lack of global dipole field on Mars and discovered the presence of inhomogeneous, locally intense crustal remanent magnetic fields [*Acuña et al.*, 1999, 2001], a remnant of a core dynamo present before ~4 Gyr ago [*Lillis et al.*, 2008, 2013]. These fields are unique to Mars among solar system bodies and their interactions with the draped interplanetary magnetic field (IMF) result in a complex magnetic topology, as evidenced by the map of the percent occurrence of open magnetic field lines (i.e., connecting the IMF to the Martian atmosphere) [*Brain et al.*, 2007]. In particular, strong and weak magnetic fields exist in close proximity, and magnetic "loops" and "cusps" stand alongside on a length scale of a few tens of kilometers [*Mitchell et al.*, 2001]. Cusps are regions where the magnetic field lines converge toward the surface, while loops are produced by the close proximity of sinks and sources of magnetic fields, e.g., upward and downward dipoles, producing arch-shaped field lines. This unique magnetic configuration has direct consequences for Martian ionospheric electrodynamics.

For example, *Withers et al.* [2005] suggested that "anomalies" in some electron profiles of MGS Radio Science experiment are linked to the orientation of the local magnetic field. *Opgenoorth et al.* [2010] investigated the dayside ionospheric conductivity at Mars and concluded on the coexistence of Earth-like conductivity profiles close to and above the strong crustal magnetic anomaly, as well as Titan-like ionospheric behavior in regions of strong radial magnetic field. *Fillingim et al.* [2007] simulated the formation of regions or "patches" of enhanced ionization in such regions of strong radial magnetic field on the nightside ionosphere. To do so, they developed an electron transport model and investigated the changes in the electron profiles due to precipitations of solar wind electrons in "plasma conduits" formed by connection of the Martian crustal fields to the IMF [*Mitchell et al.*, 2001]. *Dubinin et al.* [2008] used MGS observations to evidence the intrusion of solar wind electrons into the magnetic cusps, gaining access to the lower ionosphere down to altitudes ≤400 km.

Fillingim et al. [2010] took a closer look at the electrodynamics of a region of the ionosphere, the dynamo region, where electrons are guided by gyromotions around the magnetic field lines while ion dynamics are dominated by collisions. They estimated this region to span between ~110 and 160 km altitude. They also showed that nonuniform density profiles and neutral wind at Mars could lead to the formation of electric currents in the dynamo region, hence starting to address the questions initially raised by *Withers et al.* [2005]

about dynamo processes. In parallel, *Withers* [2008] developed a theoretical model for plasma transport and found that currents $\sim 10^{-8}$ A/m^2 were likely to form in the Martian ionospheric dynamo in a 50 nT field. *Fillingim et al.* [2012] further pursued their investigations of the wind-driven electrojets (so-termed by analogy with the auroral phenomenon on Earth) and showed that the magnetic perturbation resulting from these currents can be detectable by an orbiter, such as the Mars Atmosphere and Volatile EvolutioN (MAVEN) spacecraft [*Jakosky*, 2011], which launched 18 November 2013. MAVEN's main goal is understanding the history of the Martian volatiles [*Jakosky*, 2011]. Our research, started in *Riousset et al.* [2013], revolves around the possible role of ionospheric electrodynamics in governing ion escape.

In *Riousset et al.* [2013], we introduced a Martian Multifluid Magnetohydrodynamic (MHD) Model (M^4). We used uniform magnetic field configurations to qualitatively and quantitatively validate the model and to demonstrate the development of conduction currents in the Martian ionosphere between 100 and 250 km altitudes. Our results also showed the dependence of the dynamo currents on the magnitude of the remanent crustal field and the neutral wind speeds.

Uniform fields are an oversimplification of Mars' crustal fields, whose complexity has been successfully reproduced by several models [*Purucker et al.*, 2000; *Arkani-Hamed*, 2004; *Langlais et al.*, 2004]. Specifically, *Langlais et al.* [2004] demonstrated how an equivalent source dipole technique can be used to model the vector magnetic field $\vec{B}$ due to the remanent magnetism. They used 4840 dipoles, placed 20 km below the surface, with a mean spacing of 2.92° (~173 km), and effectively reproduced MGS's observations at ~400 km. Here we propose to use buried dipoles similar to *Langlais et al.*'s [2004] to model intense crustal magnetic field at a regional scale in order to address the question of the Martian electrodynamics in the dynamo region. We choose to neglect the contribution of the IMF draping field, as it remains $\lesssim$1–2 orders of magnitude smaller than the magnetic fields modeled in this study.

Section 1 has contextualized the present work. Section 2 will briefly summarize the salient features of our electrodynamic model and the specific parameters pertinent to the cusp and loop topologies discussed in section 3. The electric currents loop around the regions of intense magnetic field, altering the local field and the vertical motions of electrons and ions. The end of section 3 discusses the case of a series of parallel loops (which we refer to as "arcades") and its influence on the vertical fluxes of ions. These results and the scientific contributions following from this work are summed up in section 4.

2. Model Formulation

The model is described and validated in *Riousset et al.* [2013]. It differs from other plasma dynamic models at Mars in that it simulates the collisional interactions between electrons, ions, and neutrals, thus making the use of an approximate atmospheric conductivity/resistivity unnecessary. These interactions are the only ones able to generate currents, electric fields, and magnetic perturbations in the dynamo region but are not included in most existing models (e.g., *Haider et al.*'s [1992] photochemical model, *Bougher et al.*'s [2009] global circulation model, *Brecht and Ledvina*'s [2006] and *Ledvina et al.*'s [2008] semikinetic hybrid models, and *Ma et al.*'s [2002, 2004] single-fluid, multispecies MHD model). *Najib et al.* [2011] introduced ion-ion and ion-neutral collisions but neglected electron collisions, in a planetary scale, multifluid MHD model. This approximation suppresses the conditions for forming the dynamo region upper boundary and may break at altitudes $\gtrsim$250 km for studies of the dynamo region. Our model includes both electron and ion collisions to simulate the magnetohydrodynamics of atmospheric O_2^+, CO_2^+, O^+, and electrons in the multifluid framework. Planetary and solar wind H^+ have been neglected in this study of the dynamo region due to very low densities below 300 km [*Ma et al.*, 2004]. In M^4, each ion fluid is treated as an individual, yet coupled fluid, with its own density, momentum, and pressure obtained from the conservation laws and equations of state. The equation of state for electrons, assumed quasi-neutrality of the plasma, and definition of the current density are used to characterize the electron flow, which acts as a neutralizing fluid. Finally, the electric field, magnetic field, and current density are obtained from the classic electromagnetic laws (Maxwell-Faraday's, Maxwell-Ampère's, and generalized Ohm's laws) described in *Riousset et al.* [2013]. The collision terms explicitly appear in the generalized Ohm's law and in the momentum equations and are the driving force of the formation of the dynamo currents in the Martian ionosphere.

Our simulation domain is composed of two Cartesian subdomains: a uniformly discretized, high-resolution inner domain and a nonuniform outer domain, with progressive decrease in the resolution. The inner domain has dimensions 200 km × 200 km in the horizontal directions (x and y) and covers the altitude

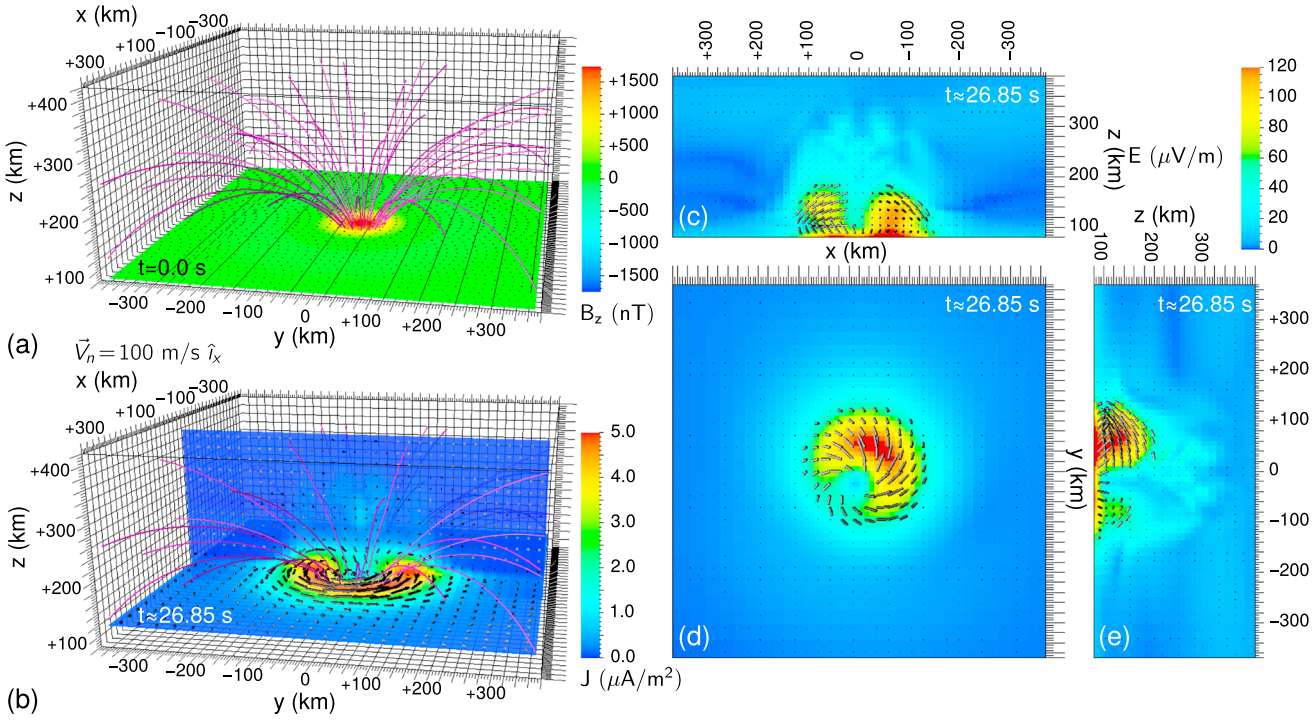

Figure 1. Results for a magnetic cusp created by a single dipole with moment $\mu = 10^{16}$ A · m^2 placed 20 km below the Martian surface. (a) Magnitude of the vertical magnetic field B_z at $t = 0$ s (color map) and magnetic field lines (solid magenta lines). (b) Magnitude (color map) and direction (solid black arrows) of the current density $\vec{J}$ in the planes $y = 0$ km and $z = 112$ km. The dynamo current is confined in the altitude range $110 \lesssim z \lesssim 150$ km. Magnitude (color map) and projected direction (solid black arrows) of the electric field $\vec{E}$ in three cut planes: (c) at $y = 0$ km, (d) at $z = 112$ km, in the dynamo region, and (e) at $x = 0$ km. In Figures 1b–1e, dark blue corresponds to zero electric field or current, while values at or above the maximum of the color bar are shown in dark red.

range between 80 and 200 km. It is discretized using $\delta x = \delta y = 10$ km and $\delta z = 4$ km space steps. The outer domain covers a total area of 13° × 13° (~800 × 800 km) centered around the inner grid and extends up to $z \approx 400$ km altitude. In this subdomain, the lengths of the discretization steps increase by 10% increments. For a domain of these dimensions, the curvature of the Martian surface is ~0.03; therefore, the curvatures effects are negligible in the framework of the current studies.

For initial conditions of all the simulations described in the following section, we use *Riousset et al.*'s [2013] horizontally uniform atmospheric profiles extrapolated down to 80 km altitude (see supporting information). We apply a uniform neutral wind flowing from $x \ll 0$ to $x \gg 0$ at 100 m/s, and similar initial flows of ions moving along the y direction. This choice maximizes the effects of collisions, which depend on the vector difference between the velocities of the neutral particles and of the charge carriers. Neglecting these collisions would make it impossible to form a dynamo region, which is the focus of our study. In addition, the model assumes balance of sources and losses of charge carriers in the continuity, momentum conservation, and pressure equations. Our combined uses of the balance of sources and losses and Neumann boundary conditions (see supporting information) reduce the range of applicability of our results to a time following the ramp-up and before depletion of the material initially present in the simulation domain. The system reaches a quasi-steady state after about $\tau \approx 5$–10 s (see section 3). Our conclusions are drawn after ~3τ to ensure that (1) the system has achieved reasonable stability and (2) it is not significantly perturbed by the reflection of Alfvén waves on the domain boundaries.

To test the magnetic cusp scenario, the initial magnetic field is produced by an upward directed magnetic dipole, with a magnetic moment $\mu = 10^{16}$ A · m^2, placed 20 km beneath the surface, consistent with the depths of the dipoles in *Purucker et al.*'s [2000] and *Langlais et al.*'s [2004] models, and the magnitude of the magnetic field at 200 km modeled by *Purucker et al.* [2000] near (15°N, 15°E) and (10°S, 110°E) where one expects to see two examples of isolated cusps. The field structure produced by this dipole is shown in Figure 1a, along with the magnitude of the vertical field B_z at $z = 80$ km. The quantity B_z corresponds to the

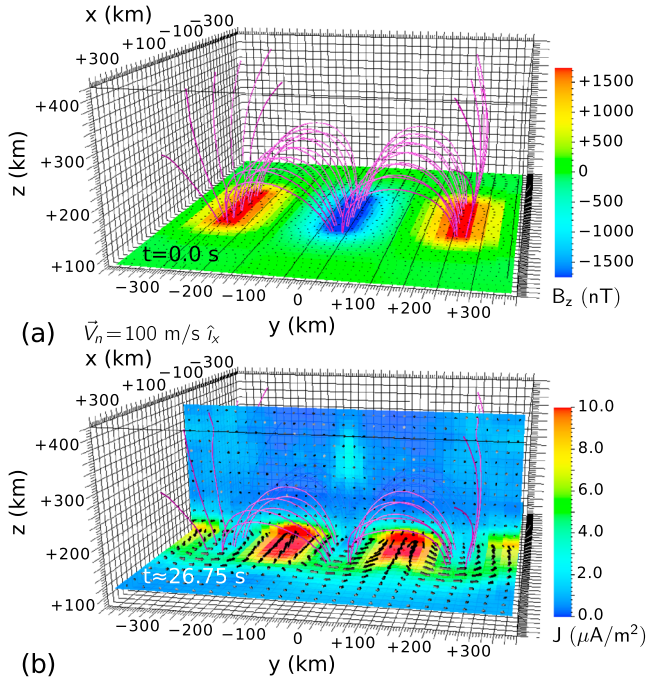

Figure 2. Results for "magnetic arcades" created by nine dipoles with the same magnetic magnitudes as in Figure 1. The dipoles are placed in three rows with alternating up/down directions. The six upward directed dipoles are placed at the coordinates (in kilometers) (−100; −250; −20), (0; −250; −20), (+100; −250; −20), and (−100; +250; −20), (0; +250; −20), (+100; +250; −20); the three downward directed dipoles are inserted in-between at (−100; 0; −20), (0; 0; −20), and (+100; 0; −20). (a) Magnitude of the vertical magnetic field B_z at t = 0 s (color map) and magnetic field lines (solid magenta lines). (b) Current density $\vec{J}$ in the planes x = 0 km and z = 112 km. The color map shows the current density magnitude while the solid black arrows indicate the current direction projected in the cut planes. As in Figure 1, the dynamo current is confined in the altitude range $110 \lesssim z \lesssim 150$ km.

radial field (normal to the planet's surface) in the representation of the Martian crustal field by *Purucker et al.* [2000] and *Langlais et al.* [2004].

Our second scenario (shown in Figure 2a) employs nine dipoles arranged in three rows of three dipoles. Each dipole has the same magnetic magnitude as the one which produced the cusp of Figure 1a. The central row (at y = 0 km) is constituted by three downward directed dipoles, 100 km apart, flanked by two rows (at $y = \pm 250$ km) of three upward directed dipoles, also 100 km apart. Altogether, the nine dipoles produce the magnetic field of Figure 2a, with arcade-shaped field lines spanning over ∼8–10° of the Martian surface and vertical component B_z ranging between −1500 and 1500 nT. Similar fields have been reported above Terra Sirenum by *Brain* [2002, p. 66], and consequently, the so-created loops can be thought as resembling a section of the magnetic topology at this location.

3. Results and Discussion

In the next paragraphs, we perform a detailed analysis of the electrodynamics around a magnetic cusp (Figure 1), created by a vertically oriented, buried dipole. This is used as a fundamental scenario, both because magnetic cusps exist as isolated structures, and also because they can be used as the building blocks toward complex structures such as the striped magnetic topology of Figure 2.

In order to understand the pattern of the electric field $\vec{E}$, we break the generalized Ohm's law (repeated in Table 1) into its Hall component $\vec{E}_1 = \vec{J} \times \vec{B}/en_e$, dependence on the ion velocities $\vec{E}_2 = -\sum_i n_i \vec{V}_i \times \vec{B}/n_e$, electron pressure gradient term $\vec{E}_3 = -\nabla P_e/en_e$, and the collision term $\vec{E}_4 = \sum_{t=i,n} m_e \nu_{te} \left(\vec{V}_t - \vec{V}_e\right)/e$. Here $\vec{J}$, $\vec{E}$, and $\vec{B}$ represent the current, electric field, and magnetic field, respectively. The quantities n_α, $\vec{V}_\alpha$, and P_α denote the number density, velocity, and pressure of the species α, where α can refer to electrons (e), ions ($i = O_2^+, CO_2^+, O^+$), or neutrals ($n = CO_2, O$). The collision frequency between two particles α and β is described by the parameter $\nu_{\alpha-\beta}$. Finally, e and μ_0 represent the elementary charge and free space permeability.

Table 1. Direction of the Contribution of Each Term $\vec{E}_\alpha$ to the Electric Field $\vec{E}$ in the Generalized Ohm's Law[a]

$\vec{E}_\alpha$	Direction of $\vec{E}_\alpha$
$\vec{E}_1 = \frac{\vec{J}\times\vec{B}}{en_e}$	$-\hat{z}$ and outward directed from the cusp
$\vec{E}_2 = -\sum_i \frac{n_i\vec{V}_i\times\vec{B}}{n_e}$	$+\hat{y}$ and $\begin{cases} +\hat{z} & \text{if } y \le 0 \\ -\hat{z} & \text{if } y \ge 0 \end{cases}$
$\vec{E}_3 = -\frac{\nabla P_e}{en_e}$	$\begin{cases} -\hat{z} & \text{if } z \le 130 \text{ km} \\ +\hat{z} & \text{if } 130 \le z \le 160 \text{ km} \end{cases}$
$\vec{E}_4 = \frac{m_e}{e}\sum_{t=i,n} \nu_{te}\left(\vec{V}_t - \vec{V}_e\right)$	$\begin{cases} \simeq \vec{0} \text{ away from the cusp} \\ \text{horizontal, CCW[b] elsewhere} \end{cases}$

[a]Generalized Ohm's law:

$$\vec{E} = \overbrace{\frac{\vec{J}\times\vec{B}}{en_e} - \sum_i \frac{n_i\vec{V}_i\times\vec{B}}{n_e}}^{-\vec{V}_e\times\vec{B}} - \frac{\nabla P_e}{en_e} + \sum_{\beta\neq e}\frac{m_e\nu_{e-\beta}}{e}\left(\vec{V}_\beta - \vec{V}_e\right)$$
$$= \vec{E}_1 + \vec{E}_2 + \vec{E}_3 + \vec{E}_4$$

[b]CCW: counterclockwise in the x-y horizontal plane.

Here we focus our analysis on the dynamo region. We note that throughout the simulation, the magnetic field perturbations remain rather small and the field is essentially that created by the magnetic dipole. Besides, we recall that by definition of the dynamo region, ion motions are driven by collisions, as confirmed by the simulated ion velocities. Shortly after the beginning of the simulation (and independently from the initial speed given to the ions), O_2^+, CO_2^+, and O^+ are entrained by the neutrals CO_2 and O and get the velocity $\vec{V}_n = 100$ m/s $\hat{x}$.

The other characteristic of the dynamo region is the plasma dynamics-driven motion of the electrons. The electron velocity $\vec{V}_e$ depends on the ion velocities $\vec{V}_i$ and local current $\vec{J}$:

$$\vec{V}_e = \sum_i \frac{n_i}{n_e}\vec{V}_i - \frac{\vec{J}}{en_e} \quad (1)$$

In the regions where the magnetic field is weak (i.e., away from the cusp axis at $x = 0$ km and $y = 0$ km), the contribution of the electric current to the motion of electrons is limited, and the electrons get their velocities from the ions via the term $\sum_i n_i\vec{V}_i/n_e$ in (1). Therefore, the vector difference $\left(\vec{V}_{i,n}-\vec{V}_e\right)$ is $\approx\vec{0}$ away from the cusp axis. Near the cusp axis, the magnetic field is stronger; therefore, the plasma dynamic effects become prominent. Consequently, the motion of the electrons is given by the $\vec{E}\times\vec{B}$ drift. Table 1 shows and details the directions of $\vec{E}$ observed in Figures 1c–1e. Since ions are demagnetized in the dynamo region, the $\vec{E}\times\vec{B}$ drift motion of electrons near the cusp is a major contributor to the formation of the counterclockwise dynamo current reported in Figure 1b.

In the half plane $y \ge 0$, we note that the contributions from the Hall term $\vec{E}_1$ and from the ion velocities $\vec{E}_2$ (see Table 1) both contribute to a downward electric field $\left(\vec{E} \parallel -\hat{z}\right)$. In the other half plane ($y \le 0$), the contributions of $\vec{E}_1$ and $\vec{E}_2$ are in opposite directions and overall reduce the magnitude of the vertical component of the electric field, ultimately resulting in the asymmetry observed in Figures 1d and 1e. If the model magnetic cusp is produced by a downward oriented, vertical dipole, instead of an upward directed one, our simulations (not presented here for the sake of brevity) show that the direction of the currents is reversed and the asymmetry mirrored through the $y = 0$ plane. In the dynamo region, the collision-driven ions are unaffected by this reversed orientation of the magnetic field's source, but the $\vec{E}\times\vec{B}$ drift, which governs the electron dynamics, is reversed. Therefore, a clockwise current was expected in the horizontal plane and is indeed produced by our simulations. With the direction reversals of both $\vec{J}$ and $\vec{B}$, the Hall term $\vec{E}_1$ of the generalized Ohm's law remains mostly outward directed from the cusp in the horizontal plane $z = 112$ km, while the contribution from the ions to the electric field $\vec{E}_2$ sees its orientation reversed and supports an upward $\vec{E}$ in the half plane $y \ge 0$ and downward elsewhere, ultimately acting to suppress $\vec{E}_1$ if $y \ge 0$ and increases it otherwise.

Using these conclusions, we analyze the case of the "arched" magnetic geometry in the remainder of this section. We use the magnetic cusp topology as the building block to model a magnetic arcade region resembling the configuration in Terra Sirenum, which presents the strongest remanent crustal magnetism on the planet [*Brain et al.*, 2007]. As a first approximation, we have modeled a striped arcade structure using nine buried dipoles (see section 2) producing the magnetic field lines displayed in Figure 2a. In the dynamo region, around $z \approx 110$ km, each upward dipole creates a counterclockwise current, while each downward

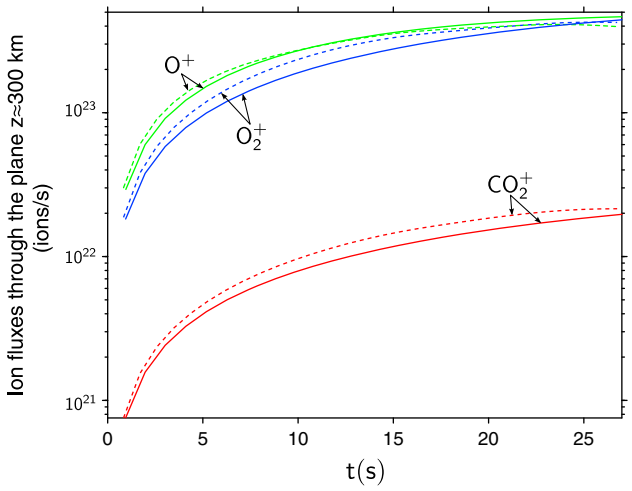

Figure 3. Ion flows above the dynamo region (through the 800 × 800 km^2 plane at $z \approx 300$ km). We plot t (s) versus F_i (#/s). Blue, red, and green lines distinguish O_2^+, CO_2^+, and O^+ fluxes, respectively. Solid lines correspond to the magnetic cusp simulation of Figure 1, while dashed lines refer to the magnetic arcade case of Figure 2.

dipole creates a clockwise current. The sum of these individual currents produces parallel dynamo currents along the x axis, moving alternatively in the $-\hat{x}$, $+\hat{x}$, and $-\hat{x}$ directions, the strongest currents being between the rows of dipoles, at $y \approx \pm 150$ km.

Current estimates suggest that up to 90% of Mars' atmosphere was lost during the Noachian period [*Jakosky and Phillips*, 2001]. Nowadays, the atmospheric pressure at the surface is <1% of that on Earth ($p_M \approx 0.6$ mbar) [*Jakosky and Jones*, 1997]. Observations indicate that the Martian atmosphere is still being lost to space, but to what extent and via which processes are questions central to NASA, as illustrated by the MAVEN program [e.g., *Folta*, 2010; *Jakosky*, 2011]. *Jedrich* [2012] summarized the processes suspected to contribute to the Martian atmospheric escape. Among these, we note that several of them are directly pertinent to ion motions (e.g., pickup ionization and ionospheric outflows due to the IMF or the crustal fields). The truly multifluid nature of our model allows us to simulate the plasma dynamics of mass-differentiated ions.

Specifically, resolving the momentum conservation equation for each ion i lets us calculate the flux, $F_i = \int\int n_i \vec{V}_i \cdot \hat{z}\, dx\, dy$, from the dynamo region to the upper ionosphere (namely, through the 800 × 800 km^2 plane at $z \approx 300$ km). Figure 3 compares the evolution of F_i versus time t during the first ~30 s of the simulation.

After the initial transient stage (~5–10 s), the fluxes through the $z \approx 300$ km plane reach a plateau ($t \gtrsim 20$–25 s). At this point, the fluxes produced in the arcade case (shown by dashed lines) remain consistently smaller than those obtained in the cusp cases (displayed using solid lines) for O_2^+ and CO_2^+ (by 10–20%), and F_{O^+} in the cusp case passes that of the arcade case at $t \geq 30$ s. This observation can be explained as follows: a cusp connects the crustal field to the IMF via open magnetic field lines diverging at higher altitudes, and therefore exposing the ionosphere to ion escape and allowing flows of ions to upper regions of the Martian atmosphere and possibly to space (see Figure 1a). On the other hand, these flows are likely to be prevented when the surface and lower atmosphere are shielded by closed field lines (i.e., attached to the atmosphere at both ends) due to the presence of magnetic loops and arcades. Figure 2a shows this shielding. Such shielding ultimately reduces the fluxes of ions from the dynamo region to the upper ionosphere although the presence of multiple sources for the arcade case produces an overall more intense magnetic field than in the case of an isolated cusp.

These effects are likely to be nuanced and refined by the addition of atmospheric dynamic chemistry, which we plan to address in detail in future work. Yet the above results represent one piece of the puzzle of the Martian atmospheric escape and a first step toward understanding the role of ions in this escape.

4. Conclusions

The principal results and contributions following from this work can be summarized as follows:

1. The dynamo current forms in a torus shape around the base of an isolated magnetic cusp due to the $\vec{E} \times \vec{B}$ drift of electrons;
2. The asymmetry in the horizontal component of the electric field is explained by the dependence of $\vec{E}$ on the collision-driven ion dynamics;

3. The organized pattern of the dynamo current produced by a striped magnetic field topology can be straightforwardly explained using the results from isolated vertically oriented, upward and downward magnetic dipoles, and the principle of superposition;
4. Strongly magnetized regions of Mars (e.g., Terra Sirenum) are likely to shield the local atmosphere and alter the motion of charged particles from the lower to the upper atmosphere.

Acknowledgments
The authors gratefully acknowledge the anonymous reviewers for their valuable feedback on the manuscript. This work was supported by the National Aeronautics and Space Administration (NASA) under grant NNX10AM88G-MFRP to the Georgia Institute of Technology.

The Editor thanks two anonymous reviewers for their assistance in evaluating this paper.

References

Acuña, M. H., et al. (1999), Global distribution of crustal magnetization discovered by the Mars Global Surveyor MAG/ER experiment, *Science*, *284*, 790–793, doi:10.1126/science.284.5415.790.

Acuña, M. H., et al. (2001), Magnetic field of Mars: Summary of results from the aerobraking and mapping orbits, *J. Geophys. Res.*, *106*, 23,403–23,418, doi:10.1029/2000JE001404.

Arkani-Hamed, J. (2004), A coherent model of the crustal magnetic field of Mars, *J. Geophys. Res.*, *109*, E09005, doi:10.1029/2004JE002265.

Bougher, S. W., T. M. McDunn, K. A. Zoldak, and J. M. Forbes (2009), Solar cycle variability of Mars dayside exospheric temperatures: Model evaluation of underlying thermal balances, *Geophys. Res. Lett.*, *36*, L05201, doi:10.1029/2008GL036376.

Brain, D. A. (2002), The influence of crustal magnetic sources on the topology of the Martian magnetic environment, PhD thesis, University of Colorado at Boulder.

Brain, D. A., R. J. Lillis, D. L. Mitchell, J. S. Halekas, and R. P. Lin (2007), Electron pitch angle distributions as indicators of magnetic field topology near Mars, *J. Geophys. Res.*, *112*, A09201, doi:10.1029/2007JA012435.

Brecht, S. H., and S. A. Ledvina (2006), The solar wind interaction with the Martian ionosphere/atmosphere, *Space Sci. Rev.*, *126*, 15–38, doi:10.1007/s11214-006-9084-z.

Dubinin, E. M., M. Fraenz, J. Woch, E. Roussos, J. D. Winningham, R. A. Frahm, A. Coates, F. Leblanc, R. Lundin, and S. Barabash (2008), Access of solar wind electrons into the Martian magnetosphere, *Ann. Geophys.*, *26*, 3511–3524, doi:10.5194/angeo-26-3511-2008.

Fillingim, M., L. Peticolas, R. Lillis, D. Brain, J. Halekas, D. Lummerzheim, and S. Bougher (2010), Localized ionization patches in the nighttime ionosphere of Mars and their electrodynamic consequences, *Icarus*, *206*, 112–119, doi:10.1016/j.icarus.2009.03.005.

Fillingim, M. O., L. M. Peticolas, R. J. Lillis, D. A. Brain, J. S. Halekas, D. L. Mitchell, R. P. Lin, D. Lummerzheim, S. W. Bougher, and D. L. Kirchner (2007), Model calculations of electron precipitation induced ionization patches on the nightside of Mars, *Geophys. Res. Lett.*, *34*, L12101, doi:10.1029/2007GL029986.

Fillingim, M. O., R. J. Lillis, S. L. England, L. M. Peticolas, D. A. Brain, J. S. Halekas, C. Paty, D. Lummerzheim, and S. W. Bougher (2012), On wind-driven electrojets at magnetic cusps in the nightside ionosphere of Mars, *Earth Planets Space*, *64*, 93–103.

Folta, D. C. (2010), Mars Atmosphere and Volatile EvolutioN (MAVEN) mission design, in *Spaceflight Mechanics 2010, Parts I-III, Advances in the Astronautical Sciences,* vol. 136, edited by D. Mortari et al., pp. 1401–1415, Univelt Inc., San Diego, Calif., 20th AAS/AIAA Space Flight Mechanics Meeting, San Diego, Calif.

Haider, S. A., J. Kim, A. F. Nagy, C. N. Keller, M. I. Verigin, K. I. Gringauz, N. M. Shutte, K. Szego, and P. Kiraly (1992), Calculated ionization rates, ion densities, and airglow emission rates due to precipitating electrons in the nightside ionosphere of Mars, *J. Geophys. Res.*, *97* (A7), 10,637–10,641, doi:10.1029/92JA00317.

Jakosky, B., and J. Jones (1997), The history of Martian volatiles, *Rev. Geophys.*, *35*(1), 1–16, doi:10.1029/96RG02903.

Jakosky, B. M. (2011), The 2013 Mars Atmosphere and Volatile EvolutioN (MAVEN) mission to Mars, EPSC Abstracts presented at EPSC-DPS Joint Meeting, Nantes, France, 2-7 Oct.

Jakosky, B. M., and R. J. Phillips (2001), Mars' volatile and climate history, *Nature*, *412*, 237–244.

Jedrich, N. (2012), Instrument design for the Mars Atmospheric and Volatile EvolutioN mission, paper presented at IEEE Aerospace Conference, Big Sky, Mont., doi:10.1109/AERO.2012.6187022.

Langlais, B., M. E. Purucker, and M. Mandea (2004), Crustal magnetic field of Mars, *J. Geophys. Res.*, *109*, E02008, doi:10.1029/2003JE002048.

Ledvina, S. A., Y. J. Ma, and E. Kallio (2008), Modeling and simulating flowing plasmas and related phenomena, *Space Sci. Rev.*, *139*, 143–189, doi:10.1007/s11214-008-9384-6.

Lillis, R. J., H. V. Frey, and M. Manga (2008), Rapid decrease in Martian crustal magnetization in the Noachian era: Implications for the dynamo and climate of early Mars, *Geophys. Res. Lett.*, *35*, L14203, doi:10.1029/2008GL034338.

Lillis, R. J., S. Robbins, M. Manga, J. S. Halekas, and H. V. Frey (2013), Time history of the Martian dynamo from crater magnetic field analysis, *J. Geophys. Res. Planets*, *118*, 1488–1511, doi:10.1002/jgre.20105.

Ma, Y.-J., A. F. Nagy, K. C. Hansen, D. L. DeZeeuw, T. I. Gombosi, and K. G. Powell (2002), Three-dimensional multispecies MHD studies of the solar wind interaction with Mars in the presence of crustal fields, *J. Geophys. Res.*, *107*, 1282, doi:10.1029/2002JA009293.

Ma, Y.-J., A. F. Nagy, T. E. Cravens, I. V. Sokolov, J. Clark, and K. C. Hansen (2004), 3-D global MHD model prediction for the first close flyby of Titan by Cassini, *Geophys. Res. Lett.*, *312*, L22803, doi:10.1029/2004GL021215.

Mitchell, D. L., R. P. Lin, C. Mazelle, H. Rème, P. A. Cloutier, J. E. P. Connerney, M. H. Acuña, and N. F. Ness (2001), Probing Mars' crustal magnetic field and ionosphere with the MGS Electron Reflectometer, *J. Geophys. Res.*, *106*, 23,419–23,428, doi:10.1029/2000JE001435.

Najib, D., A. F. Nagy, G. Tóth, and Y. Ma (2011), Three-dimensional, multifluid, high spatial resolution MHD model studies of the solar wind interaction with Mars, *J. Geophys. Res.*, *116*, A05204, doi:10.1029/2010JA016272.

Opgenoorth, H. J., R. S. Dhillon, L. Rosenqvist, M. Lester, N. J. T. Edberg, S. E. Milan, P. Withers, and D. Brain (2010), Day-side ionospheric conductivities at Mars, *Planet. Space Sci.*, *58*, 1139–1151.

Purucker, M., D. Ravat, H. Frey, C. Voorhies, T. Sabaka, and M. Acuña (2000), An altitude-normalized magnetic map of Mars and its interpretation, *Geophys. Res. Lett.*, *27*, 2449–2452, doi:10.1029/2000GL000072.

Riousset, J. A., C. S. Paty, R. J. Lillis, M. O. Fillingim, S. L. England, P. G. Withers, and J. P. M. Hale (2013), Three-dimensional multifluid modeling of atmospheric electrodynamics in Mars' dynamo region, *J. Geophys. Res. Space Physics*, *118*, 3647–3659, doi:10.1002/jgra.50328.

Withers, P. (2008), Theoretical models of ionospheric electrodynamics and plasma transport, *J. Geophys. Res.*, *113*, A07301, doi:10.1029/2007JA012918.

Withers, P., M. Mendillo, H. Rishbeth, D. P. Hinson, and J. Arkani-Hamed (2005), Ionospheric characteristics above Martian crustal magnetic anomalies, *Geophys. Res. Lett.*, *32*, L16204, doi:10.1029/2005GL023483.